Advances on microLIBS and microXRF mineralogical and elemental quantitative imaging

Cécile Fabre, Kimberly Trebus, Alexander Tarantola, Jean Cauzid, Vincent Motto-Ros, Panagiotis Voudouris

▶ **To cite this version:**

Cécile Fabre, Kimberly Trebus, Alexander Tarantola, Jean Cauzid, Vincent Motto-Ros, et al.. Advances on microLIBS and microXRF mineralogical and elemental quantitative imaging. Spectrochimica Acta Part B: Atomic Spectroscopy, 2022, 194, pp.106470. 10.1016/j.sab.2022.106470 . insu-03851942

HAL Id: insu-03851942
https://insu.hal.science/insu-03851942

Submitted on 22 Jul 2024

HAL is a multi-disciplinary open access archive for the deposit and dissemination of scientific research documents, whether they are published or not. The documents may come from teaching and research institutions in France or abroad, or from public or private research centers.

L'archive ouverte pluridisciplinaire **HAL**, est destinée au dépôt et à la diffusion de documents scientifiques de niveau recherche, publiés ou non, émanant des établissements d'enseignement et de recherche français ou étrangers, des laboratoires publics ou privés.

Distributed under a Creative Commons Attribution - NonCommercial 4.0 International License

Version of Record: https://www.sciencedirect.com/science/article/pii/S0584854722001148
Manuscript_91fc622ebef5662e5d1f718562c5987c

Advances on microLIBS and microXRF mineralogical and elemental quantitative imaging

Cecile Fabre[1], Kimberly Trebus[1,2], Alexandre Tarantola[1], Jean Cauzid[1], Vincent Motto-Ros[3], Panagiotis Voudouris[4]

[1]GeoRessources UMR 7359, Université de Lorraine-CNRS, 54000 Vandoeuvre les Nancy, France

[2] Carleton University, Ottawa ON K1S 5B6, Canada

[3] Institut Lumière Matière UMR 5306, Université Lyon 1 - CNRS, Université de Lyon, 69622 Villeurbanne, France

[4] National and Kapodistrian University of Athens, Faculty of Geology and Geoenvironment, 15784, Athens, Greece

Corresponding author: cecile.fabre@univ-lorraine.fr

Abstract

Mineralogical and petrographic studies require analytical methods capable to underline the repartition of major to trace elements within geological samples. The EPMA (Electron Probe Micro Analyzer) conventional method used for such investigation, but on restrictive zones, is on the verge to be reached by µLIBS (micro Laser-Induced Breakdown Spectroscopy) and µXRF (micro X-Ray Fluorescence) techniques allowing the elemental imaging on thin rock sections or even larger samples in only several hours. These spectroscopic methods with extremely fast acquisition speed (~10 ms/pixel) are perfectly adapted to perform multi-elemental imaging of major to trace elements down to the ppm-level. Here, on a mica schist thin section that displays a wide paragenesis of minerals, µLIBS and µXRF quantitative elemental mapping are obtained using EPMA spot analyses as internal reference compositions. We exhibit the precision of the µLIBS and µXRF quantitative elemental imaging for major and trace elements repartition in an entire thin/thick rock section. According to these oxide weight contents, a rapid mineral classification is obtained, with a good discrimination between minerals even for those with similar compositions (alumino-silicates such as andalusite and kyanite) and within a complex matrix (Fe-oxides, quartz, micas, feldspars…).

© 2022 published by Elsevier. This manuscript is made available under the CC BY NC user license
https://creativecommons.org/licenses/by-nc/4.0/

1. Introduction

Over the last twenty years, the development of new spectroscopic methods such as micro Laser-Induced Breakdown Spectroscopy (µLIBS) and micro X-Ray Fluorescence (µXRF) opened new and rapid ways to perform multi-elemental imaging of major to trace elements. µLIBS is defined by the interaction between a strongly focused pulsed laser and a target, resulting in the formation of a plasma containing excited ions and atoms [1–3]. The emission spectrum resulting from the relaxing of atoms and ions are analyzed in the UV-visible NIR range by optical spectrometers. Then the detected wavelengths can provide the qualitative composition of the sample, while the intensities of these spectra are related to the elemental concentration [4,5]. Currently, LIBS imaging is experiencing significant developments with an important increase in the number of published papers [6–13]. The recent access of benchtop µLIBS imaging system permits the access to a space-resolved elemental characterization of complex materials [10]. µXRF is a nondestructive method defined by the bombardment of X-rays on a target. X-rays ionize the atoms onto the sample and the removal of an electron (ionization) will destabilize the atoms of the investigated sample [14,15]. To stabilize the atom, an electron from a higher electronic orbital will fill the gap left by the ejection of a core electron, causing the emission of a fluorescence photon in the X-ray range. This photon has a specific energy which is characteristic of the analyzed atom [16,17]. Recent developments have allowed the commercialization of benchtop µXRF devices, to access qualitative imaging of large geological samples, with high spatial resolution (around 20 µm) [14,15]. Thus µLIBS [1–3,6,8,17–20] and µXRF [14,16,17,21] are now able to perform highly sensitive (ppm level) maps of several cm^2 with microscopic resolution in a few hours at atmospheric conditions on minerals, rocks, soils, gems and artefacts. The only constrain is to polish the sample prior the analysis. This study, like many others, shows that µLIBS and µXRF imaging is perfectly adapted to the mineralogical study of small and large crystals as well as thin and thick sections presenting complex mineralogy (e.g. alteration phases, inclusions, zoned minerals). Moreover, these spectroscopic methods can perform highly accurate images (down to the ppm level [3,21]) with extremely fast acquisition speeds (~ 10 cm^2 in several hours) without any specific sample preparation except polishing [3,17,21]. For the same duration EPMA can only map a few mm^2 and the samples need a specific carbon coating.

The visualization of composition variations within geological samples allows better understanding of mineralogical and petrological investigations. The quantitative imaging of small areas (several mm^2) using Electron Probe Micro Analysis maps (EPMA) has already been undertaken by many authors [22–27]. A user-friendly software (XMapTools) has also been developed by Lanari *et al.* [27–30] for the purpose of converting qualitative EPMA or Scanning Electron Microscopy (SEM) maps (X-ray intensities) into quantitative maps using internal standards. Individual spot measurements with chemical contents obtained with EPMA or Laser Ablation Inductively Coupled Plasma Mass Spectrometry (LA-ICP-MS) are used as references to obtain a quantitative map in oxide weights

percentage [27–30]. To the best of our knowledge, elemental quantification of geological µLIBS and µXRF maps has not yet been undertaken using this software. Thus, the present study aims to test the capabilities of this software to quantify µLIBS and µXRF by using EPMA individual analyses as compositional references. Some quantification of biological µXRF and µLIBS imaging [31–33], catalyst µLIBS imaging [34,35] as well as piezoelectric crystals µLIBS imaging [36] were undertaken, but the quantification of µLIBS and µXRF geological imaging is rarely published in the literature in particular because of the complexity handling multi-phase materials. In Earth Sciences, some recent papers relate the quantification of mineralogical abundances, but only few are dedicated to the quantification of major elements [7,9,12,18]. One can point out the study of Cugerone *et al.* on the determination of trace elements in sulfides, with µLIBS germanium quantitative mapping in sphalerite in a centimeter size area [8]. We can notice that recent publications have presented metal abundances on porphyry copper rocks obtained by using LIBS and statistical methods [7], chemical and mineralogical mapping on Platinum Group ore samples using µLIBS and µXRF [12].

The present study is one of the first to relate both the quantification of µLIBS and µXRF geological elemental maps obtained on the same geological material. The crystallographic features of the sample were also studied (Raman spectroscopy) to be compared to the different elemental distributions (µLIBS, µXRF and EPMA imaging) and EPMA spot analyses (Supp. Figure 1). First, the different chemical maps were processed by attributing a mask for each mineral. A calibration was then done independently for each mineral in order to minimize possible matrix effects. The classification of minerals and the elemental quantitative maps realized from µLIBS and µXRF techniques were compared.

2. Methods and sample

The following analytical techniques, EPMA mapping and EPMA spot analyses, and µXRF mapping were undertaken at the GeoRessources laboratory, Nancy, France. The µLIBS mapping was done at the Institut Lumière Matière in Lyon, France. The thin and thick section rocks were finely polished to obtain a flat surface, and minimize the problem of interference between the X-rays or laser beam with/on the surface.

2.1 Electron probe micro analysis

Individual spot analyses as well as micro scale maps of the samples were realized using a Cameca SX100 electron microprobe analyzer equipped with five vertical wavelength-dispersive X-ray spectrometers. The spot analyses were realized with a voltage of 15 kV, an intensity of 12 nA and a

spot size of one micrometer. These spot analyses were realized with the following elements, monochromators and standards: Na (TAP, albite), Mg (TAP, forsterite), Al (TAP, Al_2O_3), Si (TAP, wollastonite), K (LPET, orthoclase), Ca (PET, andradite), Ti (LPET, $MnTiO_3$), Cr (PET,Cr_2O_3), Mn (LIF, $MnTiO_3$) and Fe (LIF, andradite). The exact spot location of the EPMA analyses are reported in Figure 1 and the limit of detection in Table 1. To compare with the other elemental maps, semi-quantitative elementary X-ray maps of a few mm² were also realized for Na, Mg, Al, Si, K, Ca, Ti, Cr, Mn and Fe, but only on some selected minerals (kyanite and andalusite minerals). In this case, a voltage of 15 kV with a beam current of 100 nA was used.

2.2 Micro X-ray fluorescence imaging

The thin rock section was mapped by the micro X-ray fluorescence (µXRF) spectrometer M4 TORNADO from Bruker equipped with a Rh-tube and two 30 mm² EDS detectors [14]. The analyses were undertaken at a pressure of 20 millibar with a 20 µm-diameter spot of X-Ray beam-matter interaction and an acquisition speed of 10 ms per pixel and a lateral resolution of 20 µm in the X and Y directions. Detection limits are variable from ppm to wt% depending on the analyzed element [37,38]. Two different detectors were used to check the diffraction effect of the monocrystal: when the two detectors gave the same result, it was concluded that no diffraction phenomena occurred. The total number of pixels is around two million. The limit of detection for major and trace elements are reported in Table 1.

2.3 Micro laser-induced breakdown spectroscopy imaging

The µLIBS imaging was conducted with a Nd:YAG laser (1064 nm) with a 5 ns pulse duration, operating at 100 Hz with an energy of 700µJ. Laser-induced plasma were generated continuously while scanning the sample surface. The imaging experiment, recorded with a step size of 25 µm, covers the entire sample surface with one µLIBS spectrum per pixel, corresponding to an ablation crater of 15 µm in diameter. The plasma emission was collected by two quartz lenses and focused onto the entrance of two round to-linear fibre bundles (19 fibres with a 200 µm core diameter) connected to two spectrometers (Shamrock 303 and Shamrock 500, Andor Technology) equipped with intensified charge-coupled device cameras used in order to record the most relevant emission lines [18]. A homemade software, developed under the LabVIEW® environment, has allowed the automation of the scanning sequences with a predefined resolution, as well as the spectral acquisition. The measurements were conducted with an argon flow of 0.8 L/min flowing the plasma region at room temperature and at ambient pressure. The limit of detection for major and trace elements are reported in Table 1.

134

135 Table 1: Limit of detection (in ppm) obtained for the different techniques using the analytical
136 conditions reported on the text (n.d. non-determined).

	EPMA (1 µm)	µLIBS (15 µm)	µXRF (20 µm)
Fe	1 692	20	900
Mn	1 681	4	1 000
Si	509	10	2 000
Al	562	2	5 000
Ca	665	0.5	2 000
Sr	n.d	0.8	n.d.
Mg	431	0.3	40 000
Na	608	0.7	70 000
Rb	n.d	10	n.d.
K	343	4	n.d.
Ti	424	5	1 200
Cr	915	4	n.d.
P	n.d	70	n.d.
As	n.d	8	n.d.
Ga	n.d	3	n.d.
Ni	n.d	12	n.d.
Zn	n.d	5	n.d.
Zr	n.d	12	n.d.
Y	n.d	4	n.d.
La	n.d	18	n.d.

137

2.4 Sample description

In order to apprehend "classical" natural cases in terms of composition and textures, a specific well known sample was selected for this multi modal characterization validation. This rock was sampled at Thassos island (Greece) and previously largely studied by Tarantola et al. [39]. The sample (so-called KT07.01/2) presents a complex paragenesis displaying kyanite-andalusite-epidote-plagioclase-quartz-phlogopite-muscovite association and a fine-grained texture with contrasted chemical composition [39,40]. The original sample was a main 200 µm thick section, from which a conventional 30 µm thin sections of several cm^2 squares has been realized. Optical microscopy and Raman spectroscopy were used to first identify the petrographic and crystallographic characteristics of the main minerals (Figure 1), while µLIBS, µXRF and EPMA imaging, as well as EPMA individual analyses were performed to investigate the spatial distribution of major and trace elements. As thick and thin sections have been done on the same rock piece, the chemical mapping obtained by µXRF and µLIBS can be compared to validate the quantification or the mineralogical identification. It is important to note that in this study, the final size of these elemental imaging will be larger than several cm^2 (~ 9.6 cm^2 for µLIBS, ~ 8.6 cm^2 for µXRF), which is larger than those obtained by EPMA (~ 2 mm^2).

After the previous study by Tarantola et al. [39] conducted on the same rock, new petrographic observations and EPMA individual analyses were done. The sample, a mica schist rock, can be characterized as an assemblage of kyanite, andalusite (in particular viridine, a Mn-rich green andalusite), Mn rich-epidote, plagioclase, muscovite, phlogopite and quartz. Several alumino-silicates were specially selected, two Al_2SiO_5 kyanite (Ky_a and Ky_b), and one Al_2SiO_5 andalusite (And_a) crystals, for more exhaustive spectroscopic investigations using Raman (Supp. Figure 1) and EPMA mapping (Figure 2). On Ky_a is characterized by a fracture containing iron oxides inclusions that separates the mineral in the middle ; the Ky_b crystal is pokilitic (Ky_1) containing inclusions of epidote, quartz and kyanite (Ky_2) (Figure 2). Some variations in Raman fluorescence signal were previously observed with a typical signature of Cr^{3+} substitutions within kyanite [40–42] as observed in the Raman study (Supp. Figure 1).

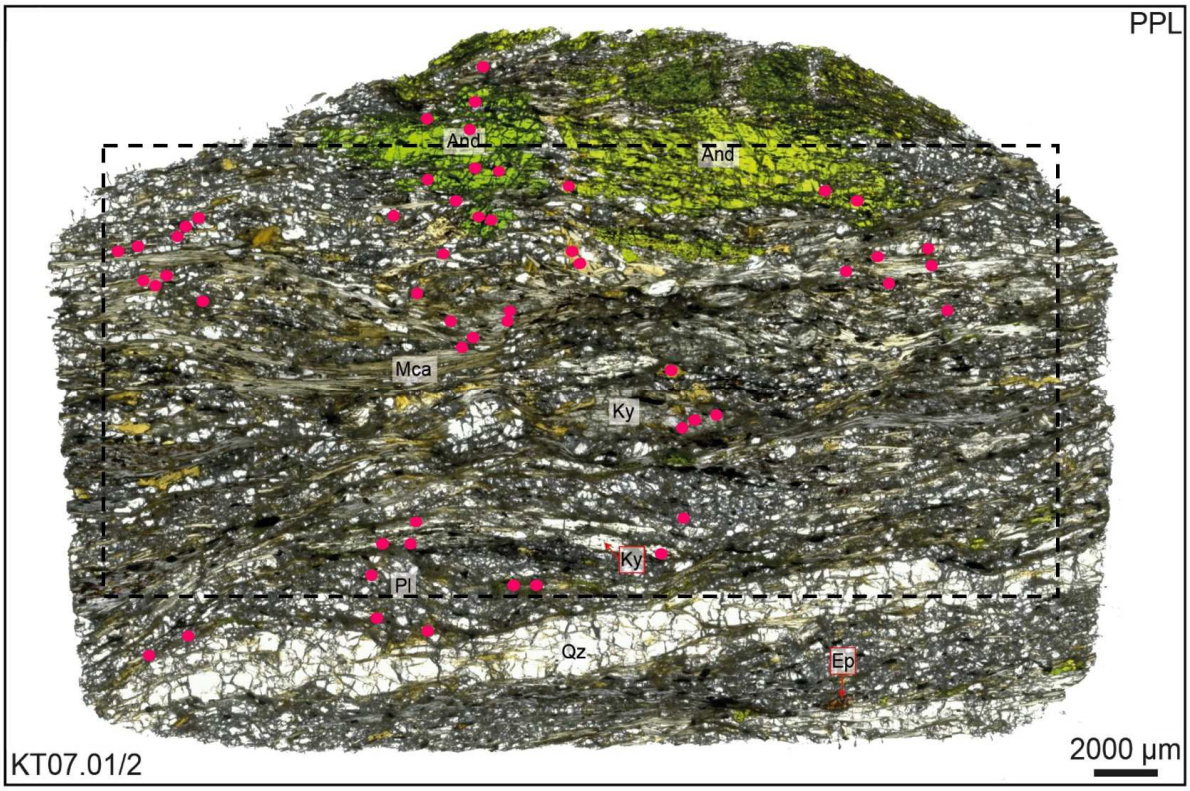

166

167 **Figure 1.** Full thick section PPL image, highlighting the presence of Mn-rich green andalusite (And),
168 micas (Mca), kyanite (Ky), plagioclase (Pl), Mn-rich pink epidote (Ep) and quartz (Qz). In this image,
169 micas with muscovite and phlogopite compositions are indistinguishable by optical analysis. The
170 dashed line square corresponds to the restricted µXRF imaging zone. The pink circles correspond to
171 the EPMA analyses.

172

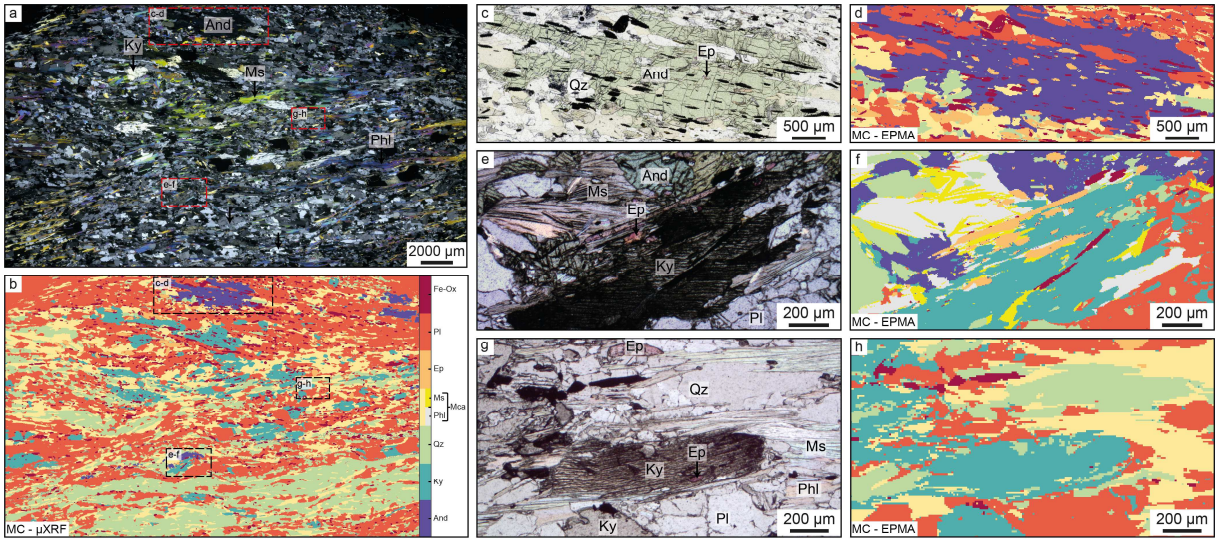

173

174 **Figure 2**. (a) Photomicrograph of the analyzed areas using µXRF on thin section with plain- (XPL),
175 (b) Mineralogical classification (MC) of (a) based on the Al, Ca, Cr, Fe, K, Mg, Mn, Na, Si, Ti and Zn

176 µXRF maps and petrographic observations: andalusite (And), kyanite (Ky), quartz (Qz), Micas (Mca),
177 epidote (Ep), plagioclase (Pl) and iron oxides (Fe-Ox). (c, e, g) Photomicrographs (PPL) of the
178 andalusite (And_a), and the two kyanite minerals (Ky_a and Ky_b); (d, f, h) Mineralogical classification of
179 the areas (d, f, h) based on the Al, Ca, Cr, Fe, K, Mg, Mn, Na, Si and Ti EPMA maps and petrographic
180 observation: andalusite (And), kyanite (Ky), quartz (Qz), Micas (Mca), epidote (Ep), plagioclase (Pl),
181 phlogopite (Phl) and iron oxides (Fe-Ox).

182

183 **2.5 Software interface**

184 XMapTools is a MATLAB based Graphical User Interface developed by Lanari et al. [27,28]. This
185 software was created firstly to convert X-ray qualitative electron microprobe or SEM maps (X-ray
186 intensities) into quantitative maps, in oxide weights percentage, by using the Castaing approach
187 (EPMA) [26,27,43]. The quantification of X-ray intensity image in XMapTools is based on a
188 calibration between the map intensity and electron microprobe quantitative individual analyses that
189 will be used as internal standards. The required data to quantify EPMA X-ray intensity maps are (i)
190 elemental maps files and (ii) a file that includes the available individual EPMA analyses (Standards)
191 with their coordinates as well as the maps coordinates. This file will be used for the standardization
192 process [29,30]. The intensities used for the calibration are those extracted from the imaging (µLIBS
193 and µXRF), pixel by pixel, meaning extracting the intensity of each element that is associated with its
194 own map. The number of these inputs is more than two million of points/pixels for both technique. For
195 µLIBS, these values correspond to the peak areas as previously described in [5,44] with the
196 description as following : the extraction method uses two spectral windows defined by the analyst
197 covering the line of interest and the surrounding background, respectively. The line area can then be
198 calculated with the difference between the signal of the peak minus and the background signal [5]. For
199 µXRF technique, the signal of the entire spectra is deconvoluted using Gaussian function, centered on
200 the theoretical position of the emission bands, and adjusted in intensity for each FWHM (full width at
201 half maximum for each element) using least squares method (PyMca X-ray Fluorescence Toolkit,
202 [45]).

203 The classification function will attribute, to each pixel of the map, a mask assignment for each mineral
204 phase, according to its chemical characteristics obtained by EPMA, µXRF or µLIBS analyses. This
205 procedure uses the k-means statistical method to classify each single pixel within a group of
206 comparable compositions. The standardization function transforms the intensities elemental maps into
207 oxide weight percent maps by using EPMA individual analyses as internal standards. Before this
208 process, various information are required for each mineral: (i) the concentration of each element in
209 oxide weight percent, (ii) their corresponding coordinates for EPMA, (iii) their intensity map
210 coordinates. To avoid any miscalculation, we used only the EPMA spot analyses in which total oxides

are superior to 90 wt%. These analyses are reported in Table 2, with the total oxide content for each spot. The values are around 93.7% and 94.5 % for the muscovite and phlogopite respectively, confirming the quality of the analyses. For the plagioclase, andalusite and kyanite minerals, these mean values are higher than 99%

The transformation of the chemical intensity maps into quantitative oxide weight percent maps involves a calibration curve for each element in each mineralogical phase that was defined during the classification process [27–29]. This way of proceeding, mineral by mineral, is essential, because it minimizes the matrix effects inherent to all analytical methods. The calibration curve is automatically defined by a line between the origin and the intercept points of the intensities and the weight composition of each standard [27–29]. As the signal background is corrected when we extract the signal for each element, the value near the origin should be close to zero. Herein, the standardization methods were applied, depending on the calibration curve optimizations and the different mineralogical phases identified in the sample.

5. MicroLIBS and MicroXRF elemental mapping

This study was done on the same mica schist rock piece. But µLIBS analysis was done on the thick rock section (map around 9.6 cm^2) and the µXRF study was done on the thin section in a smaller area than the µLIBS map (map around 8.6 cm^2). These elemental cartographies are thus larger than those obtained by EPMA (~ 2 mm^2). Nevertheless, the identification of elements and then minerals will be the same as the mineralogy of the paragenesis is identical with a fine granulometry, and then both mapping can be compared.

5.1 Elemental LIBS mapping for major and trace elements

To cover the entire thick section, about 1.5 million of spectra (pixels for each element analyzed) have been recorded using 100 Hz (~4.5 hours), with a step size of 25 µm. The selected wavelength ranges of the two detectors have been optimized for the most common major/minor elements supposed to be present in the rock. The selection of the emission lines is based on a high signal/background ratio, and possible self-absorption and interferences phenomenon were avoided [5]. The selected emission lines for the major elements are the followings: Si I 252.8 nm, Mg I 285.2 nm, Ca II 318.1 nm, Al I 308.2 nm, Na I 330.2 nm, Sr II 407.7 nm, Fe II 259.9 nm, Mn I 430.0 nm and Ti II 323.9 nm. Some other emission lines were identified and attributed to Cr I 425.4 nm, P I 255.4 nm, Zr II 327.3 nm and some Rare Earth Elements, Y II 437.4 nm and La II 408.6 nm. Typical LIBS spectra are reported in Figure 3 with the different emission lines used for the establishment of the elemental maps and then, the

mineral identification. The mean LIBS spectra are representative of each mineral phase selected, and the major elements are largely sufficient to discriminate between them (Figure 3). The oxide iron phases, minor in this paragenesis, are associated with the co-existence of Ti phases. Quartz is almost pure and the plagioclase mineral is characterized by the presence of alkaline elements (Na, Sr and Ca). Even if the kyanite and andalusite phases display the same Al_2SiO_5 composition, they can be identified and discriminated according to the high Mn content of andalusite. This observation can also be used for the interpretation of µLIBS imaging displayed in Figure 4. This figure presents the different µLIBS imaging obtained for the major elements, in the entire thick section. The colors represent the qualitative intensity of the different emission lines, selected to obtain the elemental repartition. In Figure 3 we have the net intensity recorded on the ICCD detectors in counts and in Figure 4 is not the intensity, but the net area of the selected emission lines and as the scale is used for all the minerals (the different masks), the scale is in arbitrary units. As previously seen on the optical image (Figure 1), the quartz band can be identified with the highest Si intensity in the lower part of the thin section, and for example, the kyanite are largely enriched in Mg and andalusite minerals are Mn-rich.

Looking carefully to the elemental LIBS imaging, one may notice the correlation between Al, Si and Mn (Supp. Figure 2). These correlation and the repartition of the Al, Si, Ca and Mg in the µLIBS imaging largely support the discrimination of the minerals in the sample. The most enriched Mn andalusite can be observed in the upper part of the sample. According to the Supp. Figure 3, we also see that some REE elements are also detected (La and Y seem to be correlated in terms of location), and they seem to be scattered everywhere except for the quartz. Some specific areas show high yttrium intensity. Even if zircon, titanium and phosphorus were also detected but no geological conclusions can be made. The detection limits for each element are reported in Table 1, and they are usually around or less than 1 ppm for alkaline, in the range of 10-20 ppm for Si, Fe, Rb, Ni, Zr and La and 70 ppm for P.

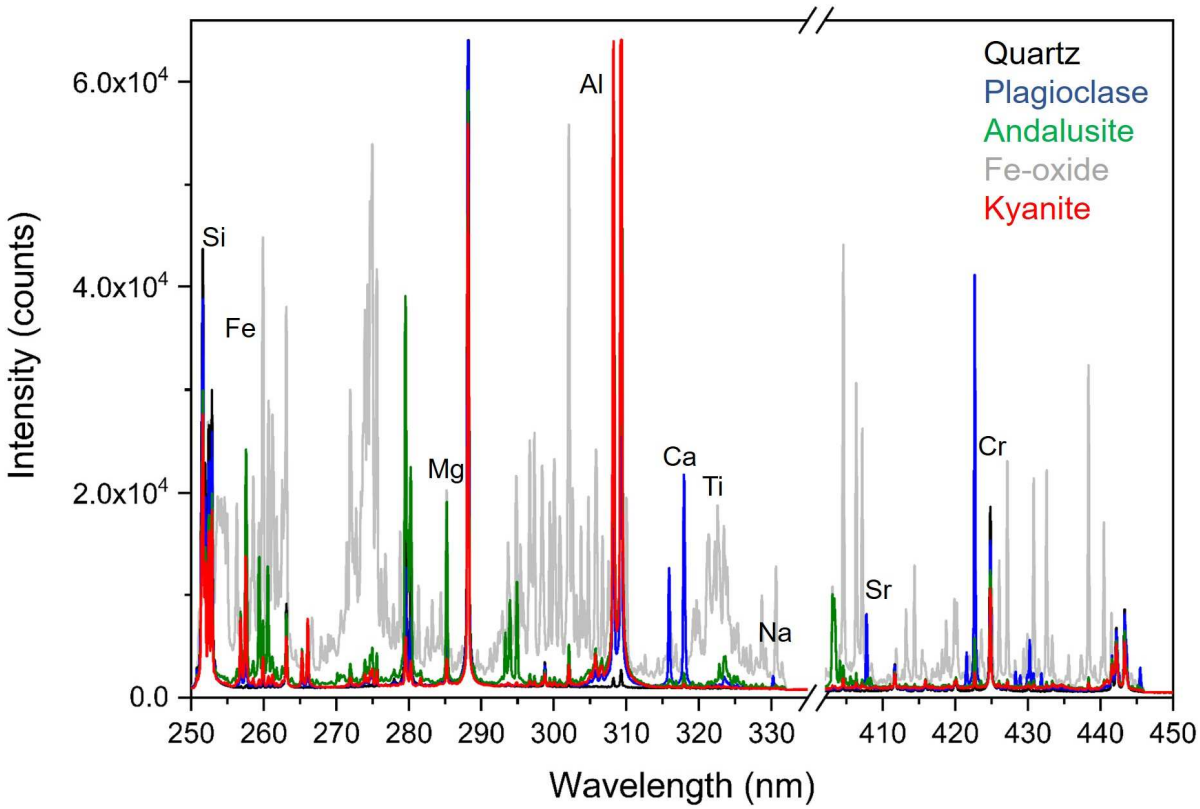

269

270 **Figure 3**. Typical LIBS mean spectra obtained on the different minerals (used as masks) observed in
271 the sample. The selected emission lines used for the µLIBS elemental imaging are also reported (Si I
272 252.8 nm, Mg I 285.2 nm, Ca II 318.1 nm, Al I 308.2 nm, Na I 330.2 nm, Sr II 407.7 nm, Fe II 259.9
273 nm, Mn I 430.0 nm and Ti II 323.9 nm, and Cr I 425.4 nm)

274

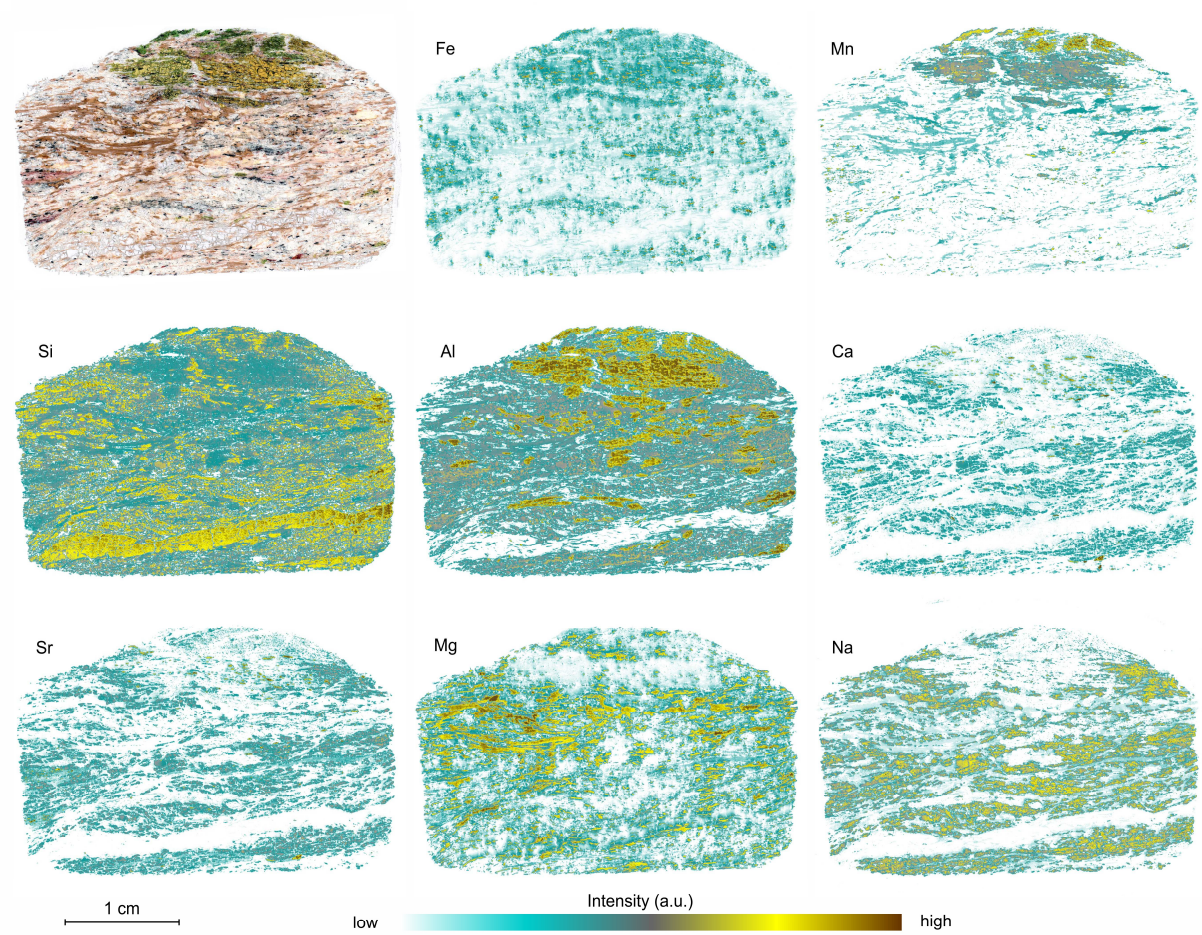

Figure 4 : µLIBS imaging obtained for major and trace elements in the thick section with a step size of 25 µm, and an ablation crater of 15 µm in diameter. The optical image of the sample is also reported to help the elemental correlation. The color scale reported in the figure is relative to each elementary image.

5.2 Elemental µXRF mapping for major and trace elements

MicroXRF maps of the entire sample were acquired in twelve hours for around 2,100,000 pixels with a resolution of 20 µm. The following elements were observed Al, As, Ca, Fe, Ga, K, Mg, Mn, Na, Ni, P, Si, Sr, Ti, and Zn. Figure 5 presents the µXRF mapping for the major/minor elements Fe-Mn-Al-Si-Ca-Mg-Sr-Na for the selected area of the thin section, and the Supp. Figure 4 is dedicated to other trace elements. The resolution of the analysis allows the distinction of the pre-supposed minerals present in the thin section, and allow either the visualization of large and small minerals with contrasted chemical components. These maps also underline some enrichments, as for example for Mn in the green andalusite crystals, even if the most enriched ones are probably identified only using the µLIBS (see next section). The limit of detection obtained for the major elements is reported in Table 2.

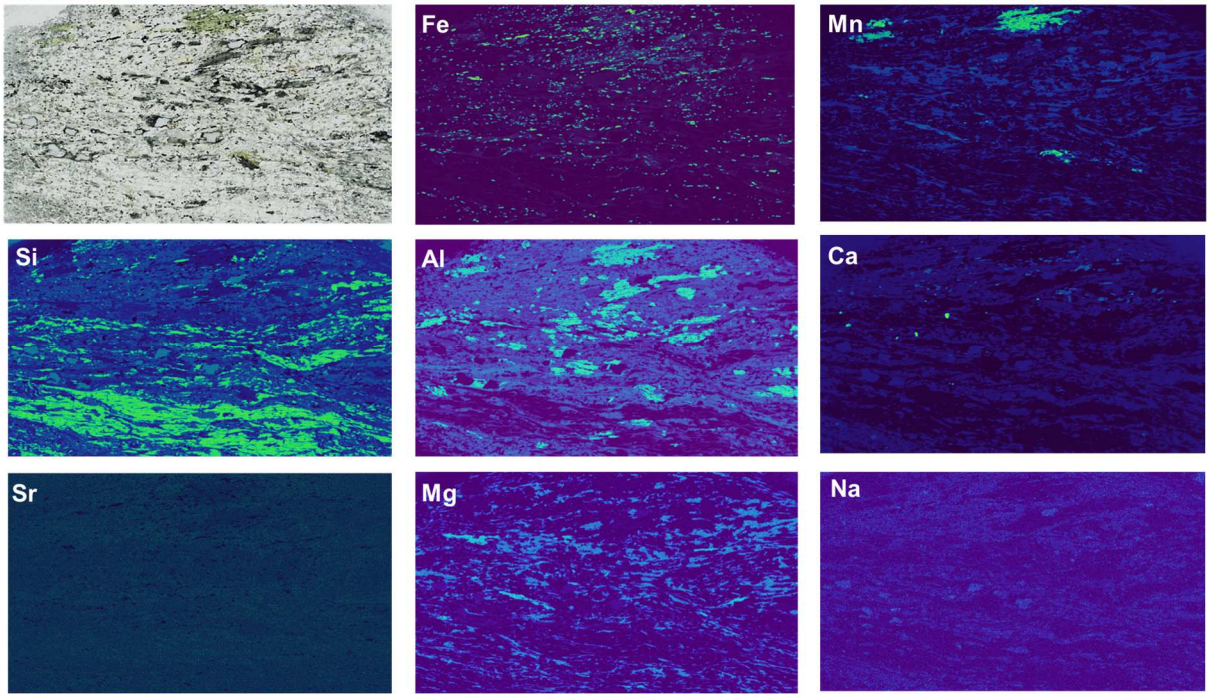

Figure 5 : µXRF elemental imaging obtained for major and trace elements in the thin section with a resolution of 20 µm. The first image corresponds to the optical view of the thin section.

5.3 Comparison between µLIBS and µXRF mapping

In these LIBS elemental mapping obtained for the Fe,-Mn,-Al,-Si,-Ca,-Mg,-Sr, and-Na elements (Figure 4), one can recognize the different minerals as already detailed in the optical view (Figure 1). For example, the quartz phase corresponds to a large zone with a Si high-constant intensity with only Mg as trace element. Plagioclase, which represents a large proportion of the small minerals of the rock matrix, can be identified with the correlation between Si and the most common alkaline elements (Na, Sr, Ca). We can emphasize that the Sr distribution in µLIBS mapping has better resolution than µXRF, and Na-Sr correlation can only be performed for this imaging. The kyanite phase is associated with high Al and Si intensities, with low amounts of Fe and Mg. In Supp. Figure 3, we can also discriminate the different andalusite crystals and specifically those with high Mn enrichment for the crystals in the upper part of the sample. In fact, the distinction between the different alumino-silicates, Al_2SiO_5 kyanite, and Al_2SiO_5 andalusite crystals can be made using the major element imaging, obtained either by µLIBS or µXRF. Kyanite crystals are discriminated with both high Al and Si intensities, with low amount of Mn or Mg, as is the case for andalusite (here viridine). Some trace elements for µXRF mapping (K-Zn-Ni-P-Ti-Ga) are reported in Supp. Fig 4, and may help for the determination of the different minerals. Even if the limit of detection for alkaline are quite high for XRF (several thousands of ppm, see Table 1), K is highly correlated with Al and Ti with Fe, which underlies the presence of phlogopite/biotite. The Fe-oxides are also associated with high-Ti intensities,

but Ti seems to be present in most of the minerals (Supp. Figures 3 and 4). For both techniques, we also observe P intensities correlated with the highest intensities of Ca in some small areas, corresponding to the presence of small apatite crystals. REE elements (La and Y) are also detected in the thick section using µLIBS, and only the quartz appears to be depleted in these elements.

5.4 Quantitative oxide mapping (µLIBS, µXRF, EPMA)

The intensities of each element have been extracted from the elemental micro imaging (elemental files) pixel by pixel, meaning spectra by spectra. Using the standardization process (see section 3.1), XMapTools which attributes composition in wt% oxide for each element, to every pixels of the imaging according to the individual EPMA analyses used as reference points (Figure 1). The mineral description process is an important procedure within the quantification of elemental maps. If minerals in a sample are not differentiated accurately, the calibration curves will not be representative of one mineralogical phase but of a mixture that will lead to inaccurate quantitative maps. Therefore, pre-knowledge of the paragenesis of the sample is recommended for a rapid and accurate classification.

Quantitative elemental distributions were investigated using either µXRF and µLIBS images for the following elements Al, Ca, Fe, Mg, Mn, Na, Si and Ti for all the area (Figure 6 and Figure 7), and on restricted area for EPMA mapping on the specific minerals andalusite and kyanite (Supp. Figures 5, 6 and 7). The elemental distribution is rather coherent between the quantitative µLIBS and µXRF maps (Figure 6 and Figure 7). However, comparing the quantitative values obtained on the andalusite mineral (Figure 8), the oxide wt % composition range is wider within the quantitative µLIBS and µXRF imaging than those obtained using the individual analyses done by EPMA. Indeed, EPMA imaging has been obtained with smaller spot analysis than for µLIBS or µXRF. An overestimation of more than 8 wt% is observed for some chemical elements: Al_2O_3 in µLIBS and µXRF maps, CaO within the µXRF quantitative map, SiO_2 (µXRF and µLIBS). The overestimation of SiO_2 is probably due to the manual calibration of quartz (and a lack of other high-Si phases in the sample). The values in CaO is relatively low, less than 0.2 wt%, thus we observe a larger composition range due to the highest detection limits using µXRF (Table 1). We also used the intensity maps from EPMA to obtain quantitative mapping on the selected minerals, the andalusite (Figure 2 and Supp. Figure 5) and the two kyanite crystals (Supp. Figure 6 and Supp. Figure 7), and we do not observe any clear chemical zonation in the minerals, except maybe for the Fe content in the kyanite Ky_b but the Fe content is lower than 2.5 wt%. For kyanite Ky_a (Supp. Figure 6), Na, Mg and Mn are hardly detected using EPMA, than for the kyanite Ky_b.

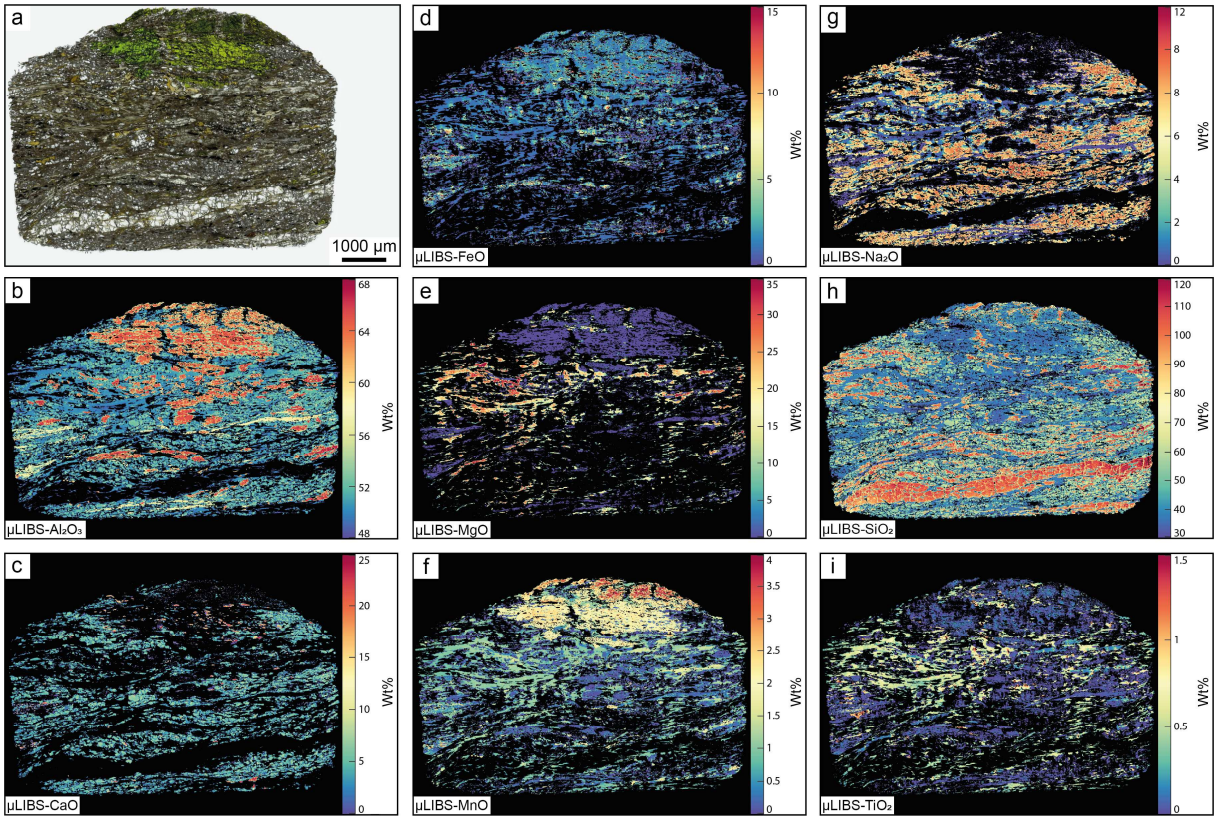

Figure 6. (a) Optical view of the thick section (PPL). µLIBS quantitative maps obtained for Al_2O_3 (b), CaO (c), FeO (d), MgO (e), MnO (f), Na_2O (g), SiO_2 (h) and TiO_2 in wt% oxide.

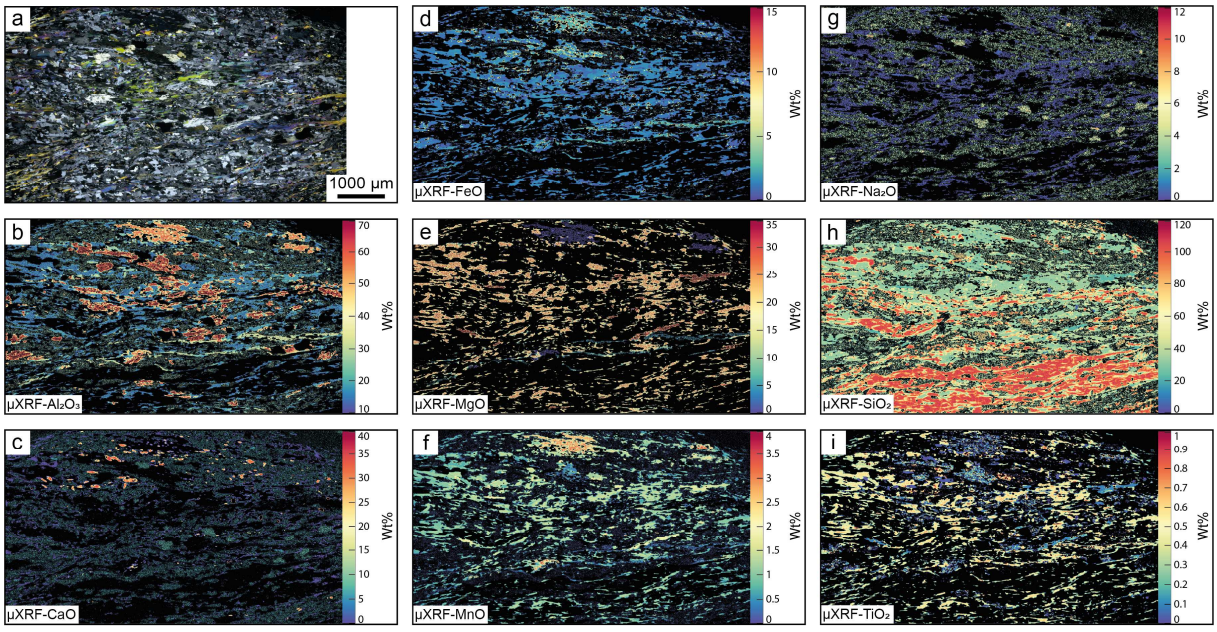

Figure 7. (a) Optical view of the thin section (XPL). µXRF quantitative maps obtained for Al_2O_3 (b), CaO (c), FeO (d), MgO (e), MnO (f), Na_2O (g), SiO_2 (h) and TiO_2 (i) in wt% oxide.

353

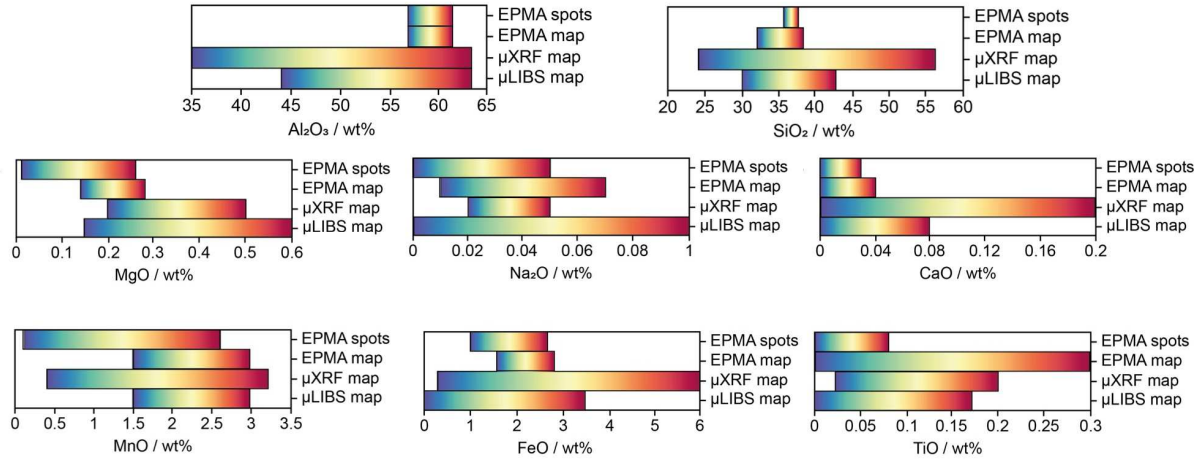

354

355 Figure 8 : Comparison of the wt % oxides obtained for the andalusite mineral phase calculated on the
356 spot analyses (EPMA) and micro mapping (EPMA, µXRF and µLIBS). The color is only indicative
357 for highest and lowest values.

358

359 Table 2 : Compositions of the different major oxides analyzed using EPMA technique, in the different mineral phases in wt% oxides and their total amount.

360 The RSD corresponds to the relative standard deviation in % for each mineral.

	Na_2O	MgO	Al_2O_3	SiO_2	K_2O	CaO	TiO_2	Cr_2O_3	MnO	FeO	ZnO	Total
andalusite_1	0.03	0.23	59.08	36.65	0.01	n.d.	0.06	n.d.	1.96	2.12	n.d.	100.13
andalusite_2	n.d.	0.23	57.9	35.6	n.d.	0.01	0.05	n.d.	2.57	1.98	0.12	98.46
andalusite_3	0.01	0.26	57.75	36.03	0.02	n.d.	0.08	n.d.	2.47	2.68	n.d.	99.29
andalusite_4	n.d.	0.24	58.85	36.25	n.d.	n.d.	0.02	n.d.	2.22	2.14	n.d.	99.71
andalusite_5	0.03	0.14	58.94	36.52	0.03	n.d.	n.d.	n.d.	2.52	1.71	n.d.	99.89
andalusite_6	n.d.	0.11	58.98	36.08	0.02	0.02	0.01	n.d.	2.25	1.74	0.14	99.36
andalusite_7	0.02	0.16	58.24	36.07	n.d.	n.d.	0.02	n.d.	2.6	1.93	n.d.	99.04
andalusite_8	0.01	0.25	57.12	37.13	n.d.	0.03	0.04	n.d.	2.16	2.16	n.d.	98.9
andalusite_9	0.01	0.19	59.17	37.16	0.01	0.02	0.01	n.d.	1.96	2.33	n.d.	100.85
andalusite_10	n.d.	0.22	58.8	37.11	0.01	n.d.	0.01	n.d.	2.07	2.1	n.d.	100.33
andalusite_11	0.05	0.22	58.42	36.84	n.d.	0.01	0.04	0.06	2.27	2.23	n.d.	100.15
andalusite_12	n.d.	0.23	58.42	36.94	n.d.	n.d.	0.05	n.d.	1.76	1.97	n.d.	99.37
andalusite_13	n.d.	0.07	59.93	36.83	0.01	n.d.	0.05	n.d.	1.8	1.05	n.d.	99.75
andalusite_14	n.d.	0.21	58.51	36.13	n.d.	n.d.	0.04	n.d.	1.72	2.07	n.d.	98.69
andalusite_15	0.02	0.17	58.15	35.68	n.d.	n.d.	0.01	n.d.	2.04	1.96	0.03	98.06
andalusite_16	n.d.	0.01	61.15	37.38	n.d.	n.d.	n.d.	0.03	0.1	0.61	n.d.	99.28
andalusite_17	n.d.	0.22	58.51	37.16	0.01	n.d.	n.d.	n.d.	2.59	2.17	n.d.	100.66
mean value	0.02	0.19	58.70	36.56	0.02	0.02	0.04	0.05	2.06	1.94	0.10	
RSD	62%	37%	2%	2%	50%	46%	63%	47%	28%	25%	61%	
epidote_1	n.d.	0.39	21.43	35.55	n.d.	20.62	n.d.	n.d.	0.88	12.51	0.07	91.45
epidote_2	0.02	0.09	23.91	37.04	0.02	22.48	0.02	n.d.	1.83	10.63	0.23	96.26
epidote_3	0.06	0.08	23.85	36.98	0.01	22.34	n.d.	n.d.	1.91	10.39	n.d.	95.62
epidote_4	0.02	0.48	21.89	36.4	n.d.	21.23	n.d.	n.d.	1.3	11.46	0.01	92.78
epidote_5	0.03	0.15	22.52	36.19	n.d.	22.44	0.03	n.d.	0.69	12.26	n.d.	94.32

epidote_6	n.d.	0.05	22.52	37.04	0.02	22.66	0.01	n.d.	1.35	11.67	n.d.	95.33
epidote_7	n.d.	0.08	22.56	37.38	n.d.	22.3	0.02	n.d.	1.94	11.48	n.d.	95.76
epidote_8	0.02	0.12	23.56	38.47	n.d.	22.61	0.01	n.d.	2.29	10.4	n.d.	97.48
epidote_9	0.05	0.15	22.62	37.96	0.02	22	0.01	n.d.	2.85	10.37	n.d.	96.01
epidote_10	n.d.	0.07	22.26	36.48	0.01	23	n.d.	n.d.	0.39	12.65	n.d.	94.86
mean value	0.03	0.17	22.71	36.95	0.02	22.17	0.02		1.54	11.38	0.10	
RSD	53%	89%	4%	2%	34%	3%	49%		49%	8%	110%	
kyanite_1	n.d.	n.d.	61.6	36.31	0.01	0.03	n.d.	n.d.	0.11	1.07	n.d.	99.13
kyanite_2	n.d.	0.05	59.74	37.01	0.01	0.04	0.01	0.03	0.12	1.1	n.d.	98.12
kyanite_3	n.d.	n.d.	62.64	37.67	n.d.	n.d.	n.d.	n.d.	n.d.	0.87	n.d.	101.18
kyanite_4	n.d.	0.01	62.37	37.62	n.d.	0.02	n.d.	0.01	0.14	0.92	n.d.	101.08
kyanite_5	0.02	n.d.	61.32	38.17	n.d.	0.01	0.02	n.d.	n.d.	0.71	n.d.	100.25
kyanite_6	n.d.	0.04	61.45	37.69	0.01	0.02	0.03	n.d.	0.03	0.85	n.d.	100.11
kyanite_7	0.01	n.d.	61.12	37.33	n.d.	n.d.	0.02	n.d.	n.d.	0.76	n.d.	99.24
kyanite_8	n.d.	n.d.	61.46	36.35	n.d.	n.d.	0.04	n.d.	n.d.	1.13	n.d.	98.99
kyanite_9	0.01	0.01	61.26	36.22	n.d.	0.02	n.d.	n.d.	0.15	1.19	n.d.	98.85
kyanite_10	0.04	n.d.	61.9	36.4	n.d.	n.d.	0.02	n.d.	0.08	0.76	n.d.	99.2
kyanite_11	n.d.	n.d.	61.29	36.68	n.d.	0.01	0.01	n.d.	0.11	1.52	n.d.	99.61
kyanite_12	n.d.	n.d.	61.29	36.86	n.d.	0.01	n.d.	n.d.	0.03	1.75	0.01	99.95
kyanite_13	0.02	0.01	62.26	36.82	0.01	0.06	n.d.	n.d.	0.04	0.61	n.d.	99.83
kyanite_14	0.03	0.02	61.41	36.55	n.d.	0.03	n.d.	n.d.	n.d.	1.4	n.d.	99.45
kyanite_15	n.d.	0.06	62.19	36.83	0.01	n.d.	0.03	n.d.	n.d.	0.71	0.05	99.89
kyanite_16	0.01	n.d.	61.39	36.3	n.d.	0.02	0.01	n.d.	n.d.	0.81	n.d.	98.53
kyanite_17	0.01	0.03	61.28	36.08	n.d.	n.d.	n.d.	n.d.	0.02	0.99	n.d.	98.41
kyanite_18	0.03	0.04	62.09	36.37	0.03	n.d.	n.d.	n.d.	0.04	0.79	n.d.	99.38
kyanite_19	0.03	0.02	61.47	36.61	n.d.	0.01	0.02	n.d.	0.05	1.39	0.18	99.78
kyanite_20	n.d.	0.03	61.95	36.91	n.d.	n.d.	n.d.	n.d.	0.1	0.8	n.d.	99.79
mean value	0.02	0.03	61.57	36.84	0.01	0.02	0.02	0.02	0.08	1.01	0.08	

RSD	52%	58%	1%	2%	61%	64%	47%	71%	58%	31%	111%	
muscovite_1	1.43	1.01	33.88	46.76	8.89	n.d.	0.44	0.02	0.05	2.75	n.d.	95.24
muscovite_2	1.43	0.98	32.23	46.53	9.08	0.03	0.35	n.d.	0.02	2.55	n.d.	93.19
muscovite_3	0.77	1.16	33.56	45.22	9.08	n.d.	0.35	n.d.	n.d.	2.71	n.d.	92.85
mean value	1.21	1.05	33.22	46.17	9.02	0.03	0.38	0.02	0.04	2.67		
RSD	31%	9%	3%	2%	1%		14%		61%	4%		
phlogopite_1	0.35	23.24	15.67	41.4	9.87	0.05	0.57	n.d.	1.01	1.39	n.d.	93.56
phlogopite_2	0.29	24.01	16.68	40.19	9.72	n.d.	0.58	n.d.	1.01	1.4	n.d.	93.88
phlogopite_3	0.39	24.14	17.23	40.23	9.53	0.04	0.53	n.d.	1.06	1.33	n.d.	94.47
phlogopite_4	0.31	24.03	17.01	40.48	9.69	n.d.	0.57	n.d.	0.97	1.35	n.d.	94.41
phlogopite_5	0.41	23.99	16.65	40.44	9.42	n.d.	0.53	n.d.	0.98	1.45	n.d.	93.88
phlogopite_6	0.37	23.25	17.32	40.01	9.45	0.01	0.6	n.d.	1.1	1.65	n.d.	93.77
phlogopite_7	0.39	24	17.69	41.13	9.42	n.d.	0.57	n.d.	0.94	1.57	n.d.	95.71
phlogopite_8	0.36	23.85	17.63	41.28	9.44	0.01	0.53	n.d.	0.84	1.6	0.1	95.65
phlogopite_9	0.37	23.61	17.51	40.62	9.59	n.d.	0.55	n.d.	1.12	1.43	n.d.	94.8
phlogopite_10	0.29	24.27	17.24	40.63	9.69	n.d.	0.55	n.d.	0.79	1.36	0.06	94.88
mean value	0.35	23.84	17.06	40.64	9.58	0.03	0.56		0.98	1.45	0.08	
RSD	12%	1%	4%	1%	2%	75%	4%		11%	8%	35%	
plagioclase_1	7.63	0.02	24.77	59.24	0.09	6.82	n.d.	n.d.	0.01	n.d.	0.05	98.62
plagioclase_2	7.32	n.d.	24.01	58.08	0.06	6.96	n.d.	n.d.	0.04	0.07	n.d.	96.54
plagioclase_3	7.54	0.01	24.09	57.63	0.07	6.78	n.d.	n.d.	0.02	n.d.	n.d.	96.15
plagioclase_4	8.06	0.01	25.01	62.29	0.09	6.2	n.d.	0.02	0.06	0.03	n.d.	101.78
plagioclase_5	7.7	n.d.	24.4	61.28	0.12	6.69	n.d.	0.06	0.11	0.05	n.d.	100.41
plagioclase_6	7.68	n.d.	25.9	60.61	0.07	7.3	n.d.	n.d.	n.d.	n.d.	n.d.	101.57
plagioclase_7	7.59	n.d.	24.79	58.77	0.04	6.87	n.d.	n.d.	0.11	0.03	0.05	98.24
plagioclase_8	7.9	n.d.	24.1	59.49	0.08	6.19	0.01	n.d.	n.d.	n.d.	n.d.	97.77

plagioclase_9	7.9	n.d.	24.26	60.58	0.07	6.18	0.01	n.d.	n.d.	0.11	n.d.	99.12
plagioclase_10	7.74	n.d.	24.22	60.46	0.09	6.24	0.01	n.d.	n.d.	0.02	n.d.	98.78
plagioclase_11	8.24	n.d.	23.69	60.4	0.08	5.48	n.d.	n.d.	0.03	n.d.	n.d.	97.92
plagioclase_12	8.02	n.d.	24.2	60.76	0.1	5.96	0.04	n.d.	0.06	0.06	n.d.	99.21
plagioclase_13	7.44	n.d.	25.17	59.9	0.06	7.1	n.d.	n.d.	n.d.	n.d.	n.d.	99.67
plagioclase_14	8	n.d.	24.3	60.47	0.09	5.82	n.d.	n.d.	0.02	0.12	n.d.	98.83
plagioclase_15	8.29	n.d.	23.59	61.03	0.07	5.63	n.d.	n.d.	0.04	n.d.	0.19	98.82
plagioclase_16	8.83	n.d.	23.31	63.7	0.1	4.49	n.d.	n.d.	0.05	0.1	n.d.	100.58
mean value	7.87	0.01	24.36	60.29	0.08	6.29	0.02	0.04	0.05	0.07	0.10	
RSD	5%	43%	3%	2%	24%	11%	86%	71%	68%	57%	84%	

361

In order to compare the quantitative maps/values obtained on the different minerals, using the three techniques, we will focus on the andalusite mineral. In andalusite, theoretically, the weight percentage of oxides should be relatively constant, and no zonation is expected for major elements. The oxide wt% contents of the analyzed elements (Al_2O_3, SiO_2, MgO, Na_2O, CaO, MnO, FeO, and TiO_2) within the andalusite mask are reported in Figure 8 and the range of weight oxide % is calculated on the entire andalusite mineral mask. As an example, Table 2 reports the mean values of oxide wt% obtained in EPMA, with the number of the analyses done on the andalusite mineral, and their relative standard deviations. The mean concentrations are quite similar with the different analytical methods, but their relative standard deviations are relatively different. In fact, the range in composition of the major elements (Al_2O_3 and SiO_2) are wider with µLIBS (43-63 wt% for Al_2O_3 and 30-42.6 wt% for SiO_2) and µXRF with 35-63 wt% and 24-56 wt% respectively, while within the EPMA maps (57-61 wt%, 32-38 wt%). These values can be compared to the andalusite standard compositions (57-61 wt% Al_2O_3 and 35.6-37.4 wt% SiO_2). These differences can be explained by the spatial resolution of the EPMA mapping which is around one micrometer, thus the identification of the minerals, even the smallest ones, can be done more successfully as the analyses/pixels are representative of unique mono-mineral phase. On the contrary, given the spatial resolution of 15 and 20 µm, respectively for µLIBS and µXRF imaging, the analyses performed can lead to a combination of several minerals, especially on the crystal borders. For the case of MgO and Na_2O, the µXRF quantitative estimates might not be accurate due to the high detection limit for these elements and their very low content in andalusite (<0.5 wt%). The larger ranges observed by µLIBS can also be related to the analysis of smaller minerals, with higher alkaline contents at the border or in some fractures as these andalusite crystals are poikilitic, and they are related to post-deformation and may contain many mineral inclusions. However, the mean value of the wt % oxides are still in great agreement for all the techniques even for the very low contents, lower than 0.05 wt % for CaO and Na_2O.

6. Mineralogical mapping

The mineral classification realized on the µLIBS, µXRF (Figure 9, Figure 10) and EPMA maps for andalusite crystal (Figure 2) were very similar, with the same proportion of the minerals, even if the considered areas were not exactly on the same part of the rock section. The classification of minerals has been successful for the three techniques, with the identification of all the expected minerals as andalusite, kyanite, quartz, micas (phlogopite and muscovite), epidote, plagioclase and iron oxides were categorized. It can be noted that apatite minerals were also identified using Ca and P mapping, but they are not recognized in the mineralogical classification, due to their low proportion in the sample (only a few small minerals) and a lack of EPMA spot analyses to make an apatite mask. Although, phlogopite ($KMg_3AlSi_3O_{10}(OH,F,Cl)_2$) and muscovite ($(KAl_2(AlSi_3O_{10})\ (OH,F)_2$) are both

observed in the mapped areas, these minerals were only considered as separated phases within the EPMA and µXRF maps, while for µLIBS they were categorized in the same mineralogical mask (i.e. micas) (Figure 9, Figure 10). The classification function was able to separate the two alumino-silicates, andalusite (Al_2SiO_5) and kyanite (Al_2SiO_5) which only differ by their trace element composition. Here, andalusite crystals are enriched in Mn and Mg with respectively MnO (0.05 wt% for kyanite and 2 wt% for andalusite) and MgO (0.016 wt% for kyanite and 0.19 wt% for andalusite) mean contents. However, the kyanite and andalusite are large sized crystals that are mostly separated by other phases. This is not the case of phlogopite and muscovite, which are grouped together in the rock foliation, and they remain in the same mineralogical mask for the µLIBS data. Here, the main chemical differences between phlogopite and muscovite are the MgO (about 1 wt% in muscovite and 24 wt% in phlogopite) and Al_2O_3 (about 33 wt% in muscovite and 17 wt% in phlogopite) amounts. In fact, muscovite seemed to be an alteration phase at the contact between kyanite and/or phlogopite and is thus present in small amounts compared to phlogopite. For these minerals, the selected gravity center (selected pixel on the map) and the difference in composition were probably too close to ensure a correct classification of these minerals, however all the micas are distinguished as a unique phase in the µLIBS imaging (Figure 9) and distinguished for the µXRF (Figure 10).

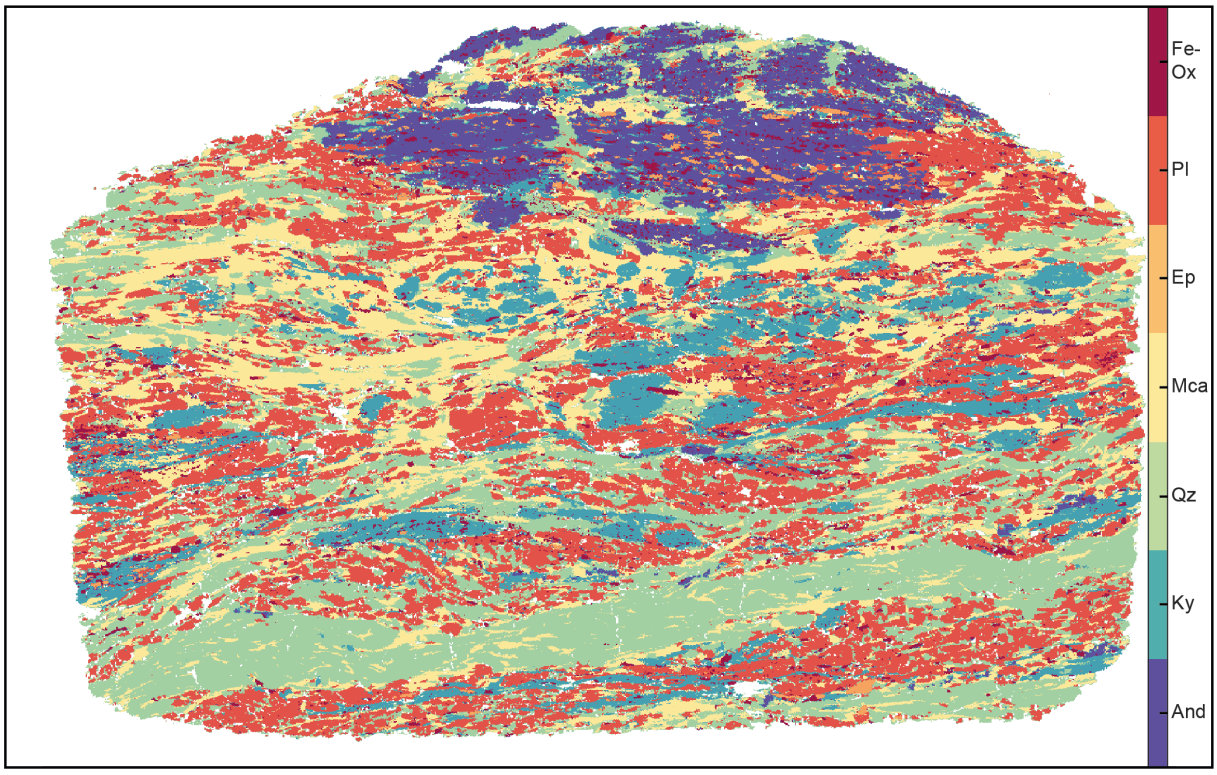

Figure 9. Mineralogical classification on the thick section, based on the Al, Ca, Fe, Mg, Mn, Na, Si, and Ti µLIBS elemental images and petrographic observation. Seven mineral phases were categorized, andalusite (And), kyanite (Ky), quartz (Qz), Micas (Mca), epidote (Ep), plagioclase (Pl) and iron oxides (Fe-Ox).

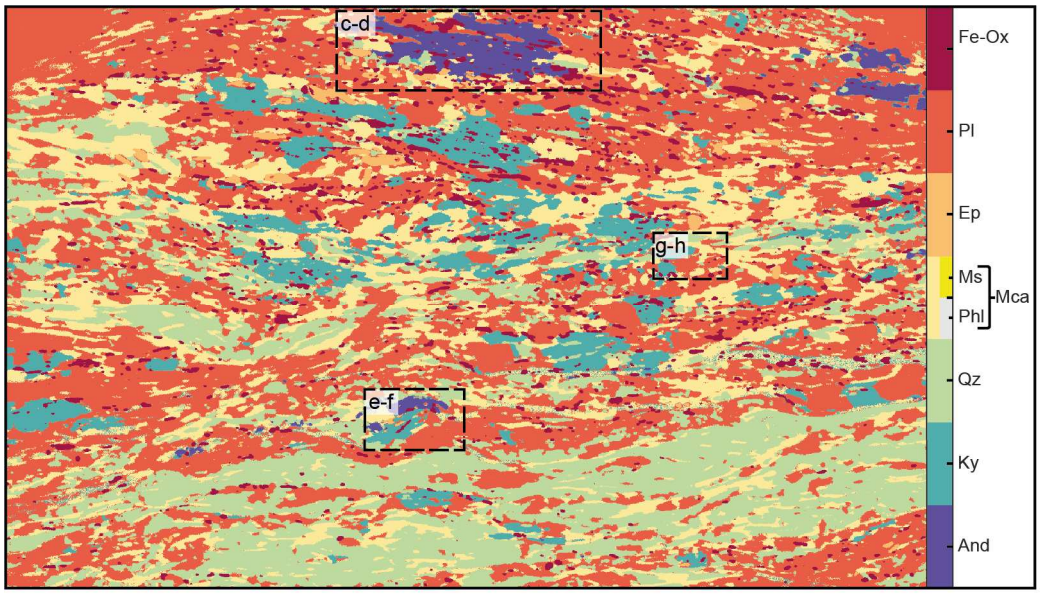

Figure 10. Mineralogical classification on the thin section, based on the Al, Ca, Cr, Fe, K, Mg, Mn, Na, Si, Ti and Zn µXRF elemental images and petrographic observation. Eight mineral phases were categorized, andalusite (And), kyanite (Ky), quartz (Qz), Micas (Mca) with muscovite and phlogopite discrimination, epidote (Ep), plagioclase (Pl) and iron oxides (Fe-Ox).

7. Discussion

7.1 Optimization of calibration process to produce quantitative elemental imaging

Pre-knowledge about the paragenesis of the sample is essential for an accurate classification. If the minerals are not differentiated accurately, this may lead to inaccurate quantitative maps. Herein, the classification was based on previous petrographic observations as well as on the chemical information that were provided by EPMA, µLIBS and µXRF imaging and EPMA individual analyses. The XMapTools classification function was applied on the different available elemental images. Broadly, the classification of the different minerals is very similar to the other spectroscopic methods, even if some elements are close to their detection limits (e.g. Mg and Na for µXRF, Ti and Cr for EPMA). An example of non-classification is the case of apatite minerals. They have been identified using the elemental mapping of Ca and P, but as they were not before identified among the paragenesis (and analyzed by EPMA for the establishment of the calibration curves), they are not identified in the mineral classification. Nevertheless, it is possible to classify the minerals by only studying the elemental analyses of a sample.

The calibration process requires high-precision internal standards for every mineral phase to guarantee the precision of the final quantitative maps [27–30]. It is important to be extremely cautious during this process to ensure that the optimal calibration curves are used. All the calibration have been done using the spot EPMA spot analysis (with an analyzer beam around 1 micrometer) that can be considered as actual standard values of the different minerals with no chemical mixing. The EPMA, µXRF and µLIBS calibration curves of major elements (particularly Al and Si) are similar (Supp. Figures 8 and 9). However, the EPMA relative intensities of these elements are 10 (Si) to 100 (Al) times higher in comparison to other elements (Mg, Ca, Na, Mn, Ti), while for µXRF and µLIBS the relative intensities are similar or lower compared to other elements. This disparity highlights that EPMA is extremely sensitive for major elements, which is not always the case for µXRF and µLIBS as their sensibility is not directly linked to the elemental concentration but will depend on the selected emission lines, according to the detector wavelength ranges. Therefore, the ranges of composition obtained within the µLIBS and µXRF quantitative maps are wider than for EPMA, allowing the access of minor to major contents in a unique analysis. The different limits of detection for EPMA, µLIBS and µXRF imaging are reported in Table 1. They were calculated based on the experimental configuration and analytical conditions of the mapping, and are not related to the use of the quantification process used in this study (XMapTool). LIBS presents the lowest values for all the alkaline contents. EPMA has the highest detection limits (due to its smaller spot size), but since the analyses were performed on alumino-silicate phases, qualitative or mineralogical imaging can be largely validated for major elements. The µLIBS, µXRF (Supp. Fig. 10 and 11) and EPMA calibration of Fe, Ca, Mg, Na and Mn, done without the outlier points, seem to be alike. But in comparison with the EPMA calibration curves, it appears that Na and Ca µXRF calibration process is more accurate than µLIBS, while Mg, Fe and Mn µLIBS seem to be better calibrated than for µXRF. The Ti calibration is efficient with µLIBS and µXRF, whereas the EPMA flat calibration curve suggested that this element is close to the EPMA detection limit and only observed at the same concentrations on the individual points, not preventing the establishment of a good calibration. As it was previously described, the detection limit of the Ti individual analyses is around 0.04 wt%, while for µLIBS it is less than 0.02 wt%. One may consider that these results are largely satisfying regarding the low amount of Ti. In the present study, quantitative maps of major elements (e.g. Al_2O_3, SiO_2) remain the most accurate with the conventional EPMA technique, while for trace and light elements this accuracy appears to be better with µLIBS and µXRF. In the present study, quantitative maps of the major elements of the alumino-silicate minerals (e.g. Al_2O_3, SiO_2) remain the most accurate with the conventional EPMA technique due to its small spatial resolution (small pixel), while for trace and light elements this accuracy appears to be better with µLIBS and µXRF due to their low detection limits.

475

476 **7.2 Contributions and comparison of the quantitative imaging**

477 The quantification of elemental maps is fundamental for geological research and industrial
478 applications. The quantification of EPMA maps has already been described by few authors [22–27]
479 but only on restricted areas of a rock section. In a previous study, we have developed a first approach
480 combining XRF and LIBS elemental imaging in a mono crystal of kyanite combined with Raman and
481 Cathodoluminescence [40]. Here, for a more complex mineralogy, the quantification of µLIBS and
482 µXRF maps seemed thus to be essential for the future development of these spectroscopic methods.
483 These fast micro-mapping done on large surfaces, with a million of pixels at the thin section scale can
484 be of first interest prior to any other more localized study, for example EPMA imaging in selected
485 zones/minerals. The quantification of µLIBS in geological studies has already been undertaken on a
486 porphyry copper rock by El Haddad et al. [7], while for XRF in our knowledge, it has only been
487 described for synchrotron XRF [46] in very small areas. The paper of El Haddad et al. [7] is the first to
488 quantify mineral abundance within LIBS maps, followed by several studies on platinoid purposes
489 [9,12]. Concerning this previous study [7], the data were classified within different mineralogical
490 phases with a Quantitative Mineral Analysis (QMA) instrument used on EDS-SEM maps and treated
491 with the multivariate curve resolution alternating least squares (MCR-ALS) method [7,47].

492 Herein, the purpose was to quantify elemental µXRF and µLIBS by using internal standards which is
493 rarely done on the same geological samples. An example of quantitative elemental maps was done for
494 germanium content in one phase, sphalerite, using spot EPMA spot analyses [8]. Here, as in the paper
495 of Nardecchia et al. [48], a k-means classification of the different mineralogical phases was performed.
496 However, in their latest paper [49] a successive k-means clustering method was applied to the LIBS
497 data, which allowed them to generate several sub-groups within every mineralogical phase. The sub-
498 group clustering process could be extremely interesting for zoned minerals, inclusions, or alteration
499 processes in quantitative or mineralogical maps.

500 The calibration process of µXRF µLIBS imaging was undertaken for each mineralogical phase with
501 internal standards, assuming no matrix effects [26,27]. Nevertheless, in some specific zoned minerals,
502 as the common case of garnet mineral, a strong composition variation between the core and the rims
503 can generate matrix effects, which can be avoided by creating a mineralogical mask for the borders
504 and the core of the mineral [27]. Moreover, after Lanari et al. [27], it is critical to guarantee that the
505 analyzed volume is similar between the standards and the calibrated maps. The analyzed volume of
506 µLIBS and EPMA are a ratio of 200, explaining some discrepancy between the weight oxide contents.
507 Furthermore, since µLIBS is a destructive technique (ablation of a few µm depending on the matrix
508 [3]) it should be applied after any other technique, as EPMA and µXRF are nondestructive methods.
509 One may underline that the XRF analysis is not exactly done vertically compared to the sample

surface. However, herein, these differences in volume do not seem to impact the calibration process of µLIBS data, which are usually equivalent to µXRF one. Moreover, in other studies [34,35], EPMA and µLIBS are used together for the calibration and we can assume that the volume variation between EPMA and µLIBS can be limited for such investigation, if the analyses remain in the same mineralogical phase. Different mineralogical classification methods of LIBS and µXRF maps are described in the literature [7,17,49,50].

It is important to mention that by a lack of individual analyses, the classification of some minerals might be inaccurate. Nevertheless, as these minerals do not present any chemical zonation, and thus lead us to consider these maps as accurate. To avoid the problem of non-discrimination of close-composition minerals, it is possible to test another classification method, evolving biplot and/or triplot module to select the pixel of the different minerals [28–30].

8. Conclusion

The main objective of this work was to perform accurate quantitative µLIBS and µXRF images by using EPMA internal standards and have access to mineralogical maps. The user-friendly XMapTools interface is perfectly adapted to perform such classification and quantification processing of images containing higher than millions of µLIBS or µXRF spectra. We demonstrated that the calibration of µLIBS and µXRF were close or even better for light and trace elements than for EPMA, which is extremely promising for the further development and use of these analytical techniques. This work also demonstrated that µLIBS and µXRF are robust tools to realize elemental images of minor and trace elements (down to ppm level) within entire thin or thick sections (about 10 cm^2) in a few hours in complex material, with minerals displaying close or contrasted chemical compositions. Even if the oxide composition range obtained within the µLIBS and µXRF quantitative images are wider than for EPMA, due to the border effects, and mixing of different composition, they are in very good agreement. Yet, these techniques provide access to minor and major content in a single, rapid analysis, as well as quantitative content and access to mineralogical imaging over large areas. The use of LA-ICP-MS on reference points, identified as internal standards, could be of great interest for certain elements difficult to detect by EPMA (ultra-trace or light elements). For further geological applications, it is important to use such large investigation (using µXRF or µLIBS imaging) to highlight the most interesting areas of the sample, prior to any more expensive or time-consuming technique in these specific zones or minerals. To verify the interest of this new working methodology, other tests will be carried out on samples coming from different geological contexts, and in particular for the case of zoned minerals (such as garnets) in order to better valorize the quantitative mapping of oxides in the growth zonations.

Credit author Statement

Cécile Fabre: Conceptualization, Methodology, Writing- Reviewing and Editing, Funding acquisition, Visualization, Validation. **Kimberly Trebus**: Resources, Writing- Original draft preparation, Visualization, Software, Investigation, Writing- Reviewing. **Alexandre Tarantola**: Resources, Conceptualization, Supervision, Visualization, Investigation, Writing- Reviewing. **Jean Cauzid**: Investigation, Conceptualization, Software, Validation, Writing- Reviewing. **Vincent Motto-Ros**: Investigation, Validation, Visualization, Writing- Reviewing. **Panagiotis Voudouris:** Resources, Writing- Reviewing.

Acknowledgments

This research was funded by Extra&Co and ICEEL Carnot with the AMELLIBS and CECILE projects respectively. We thank Alexandre Flammang and Olivier Rouer for the quality of sample preparation and EPMA analyses and Marie-Camille Caumon for the Raman analysis.

References

[1] L. Jolivet, M. Leprince, S. Moncayo, L. Sorbier, C.-P. Lienemann, V. Motto-Ros, Review of the recent advances and applications of LIBS-based imaging, Spectrochim. Acta Part B At. Spectrosc. 151 (2019) 41–53.

[2] V. Motto-Ros, S. Moncayo, C. Fabre, B. Busser, LIBS imaging applications, in: Laser-Induc. Breakdown Spectrosc., Elsevier, 2020: pp. 329–346.

[3] C. Fabre, Advances in Laser-Induced Breakdown Spectroscopy analysis for geology: A critical review, Spectrochim. Acta Part B At. Spectrosc. (2020) 105799.

[4] J. El Haddad, L. Canioni, B. Bousquet, Good practices in LIBS analysis: Review and advices, Spectrochim. Acta Part B At. Spectrosc. 101 (2014) 171–182. https://doi.org/10.1016/j.sab.2014.08.039.

[5] V. Motto-Ros, S. Moncayo, F. Trichard, F. Pelascini, Investigation of signal extraction in the frame of laser induced breakdown spectroscopy imaging, Spectrochim. Acta Part B At. Spectrosc. 155 (2019) 127–133. https://doi.org/10.1016/j.sab.2019.04.004.

[6] M. Gaft, Y. Raichlin, F. Pelascini, G. Panzer, V. Motto Ros, Imaging rare-earth elements in minerals by laser-induced plasma spectroscopy: Molecular emission and plasma-induced luminescence, Spectrochim. Acta Part B At. Spectrosc. 151 (2019) 12–19. https://doi.org/10.1016/j.sab.2018.11.003.

[7] J. El Haddad, E.S. de Lima Filho, F. Vanier, A. Harhira, C. Padioleau, M. Sabsabi, G. Wilkie, A. Blouin, Multiphase mineral identification and quantification by laser-induced breakdown spectroscopy, Miner. Eng. 134 (2019) 281–290.

[8] A. Cugerone, B. Cenki-Tok, E. Oliot, M. Muñoz, F. Barou, V. Motto-Ros, E. Le Goff, Redistribution of germanium during dynamic recrystallization of sphalerite, Geology. 48 (2020) 236–241. https://doi.org/10.1130/G46791.1.

[9] K. Rifai, L.-Ç. Özcan, F.R. Doucet, K. Rhoderick, F. Vidal, Ultrafast Elemental Mapping of Platinum Group Elements and Mineral Identification in Platinum-Palladium Ore Using Laser Induced Breakdown Spectroscopy, Minerals. 10 (2020) 207. https://doi.org/10.3390/min10030207.

[10] V. Motto-Ros, S. Moncayo, C. Fabre, B. Busser, LIBS imaging applications, in: Laser-Induc. Breakdown Spectrosc., Elsevier, 2020: pp. 329–346. https://doi.org/10.1016/B978-0-12-818829-3.00014-9.

[11] A. Limbeck, L. Brunnbauer, H. Lohninger, P. Pořízka, P. Modlitbová, J. Kaiser, P. Janovszky, A. Kéri, G. Galbács, Methodology and applications of elemental mapping by laser induced breakdown spectroscopy, Anal. Chim. Acta. 1147 (2021) 72–98. https://doi.org/10.1016/j.aca.2020.12.054.

[12] N. Mohamed, K. Rifai, S. Selmani, M. Constantin, F.R. Doucet, L.Ç. Özcan, M. Sabsabi, F. Vidal, Chemical and Mineralogical Mapping of Platinum-Group Element Ore Samples Using Laser-Induced Breakdown Spectroscopy and Micro-X-Ray Fluorescence, Geostand. Geoanalytical Res. (2021) ggr.12385. https://doi.org/10.1111/ggr.12385.

[13] J. Klus, P. Mikysek, D. Prochazka, P. Pořízka, P. Prochazková, J. Novotný, T. Trojek, K. Novotný, M. Slobodník, J. Kaiser, Multivariate approach to the chemical mapping of uranium in sandstone-hosted uranium ores analyzed using double pulse Laser-Induced Breakdown Spectroscopy, Spectrochim. Acta Part B At. Spectrosc. 123 (2016) 143–149. https://doi.org/10.1016/j.sab.2016.08.014.

[14] S. Flude, M. Haschke, M. Storey, Application of benchtop micro-XRF to geological materials, Mineral. Mag. 81 (2017) 923–948. https://doi.org/10.1180/minmag.2016.080.150.

[15] A.V. Garmay, K.V. Oskolok, O.V. Monogarova, Improved Accuracy of Multicomponent Samples Analysis by X-Ray Fluorescence Using Relative Intensities and Scattered Radiation: A Review, Anal. Lett. 53 (2020) 2685–2699. https://doi.org/10.1080/00032719.2020.1751651.

[16] T. Yamasaki, Identification of geochemical signatures associated with seafloor massive sulfide mineralization at the Iheya North Knoll, middle Okinawa Trough, J. Geochem. Explor. 188 (2018) 55–72. https://doi.org/10.1016/j.gexplo.2018.01.008.

[17] W. Nikonow, D. Rammlmair, J.A. Meima, M.C. Schodlok, Advanced mineral characterization and petrographic analysis by μ-EDXRF, LIBS, HSI and hyperspectral data merging, Mineral. Petrol. 113 (2019) 417–431. https://doi.org/10.1007/s00710-019-00657-z.
[18] J.O. Cáceres, F. Pelascini, V. Motto-Ros, S. Moncayo, F. Trichard, G. Panczer, A. Marín-Roldán, J.A. Cruz, I. Coronado, J. Martín-Chivelet, Megapixel multi-elemental imaging by Laser-Induced Breakdown Spectroscopy, a technology with considerable potential for paleoclimate studies, Sci. Rep. 7 (2017) 5080. https://doi.org/10.1038/s41598-017-05437-3.
[19] M. Rossi, M. Dell'Aglio, A. De Giacomo, R. Gaudiuso, G.S. Senesi, O. De Pascale, F. Capitelli, F. Nestola, M.R. Ghiara, Multi-methodological investigation of kunzite, hiddenite, alexandrite, elbaite and topaz, based on laser-induced breakdown spectroscopy and conventional analytical techniques for supporting mineralogical characterization, Phys. Chem. Miner. 41 (2014) 127–140.
[20] K. Trebus, A. Tarantola, C. Fabre, M.-C. Caumon, C. Jean, V. Motto-Ros, A. Lecomte, C. Peiffert, P. Voudouris, C. Mavrogonatos, Trace Element Distribution in Zoned Kyanite of Thassos Island (Greece) Using Combined Spectroscopic Analyses, Appl. Spectrosc. (2022) 00037028221108758. https://doi.org/10.1177/00037028221108758.
[21] N. Potter, N. Brand, Application of micro-XRF to characterise diamond drill-core from lithium-caesium-tantalum pegmatites, ASEG Ext. Abstr. 2019 (2019) 1–4. https://doi.org/10.1080/22020586.2019.12073139.
[22] K.F. Heinrich, Concentration mapping device for the scanning electron probe microanalyzer, Rev. Sci. Instrum. 33 (1962) 884–884.
[23] W. Jansen, M. Slaughter, Elemental mapping of minerals by electron microprobe, Am. Mineral. 67 (1982) 521–533.
[24] M.J. Kohn, F. Spear, Retrograde net transfer reaction insurance for pressure-temperature estimates, Geology. 28 (2000) 1127–1130.
[25] G.L. Clarke, N.R. Daczko, C. Nockolds, A method for applying matrix corrections to X-ray intensity maps using the Bence–Albee algorithm and Matlab, J. Metamorph. Geol. 19 (2001) 635–644.
[26] V. De Andrade, O. Vidal, E. Lewin, P. O'brien, P. Agard, Quantification of electron microprobe compositional maps of rock thin sections: an optimized method and examples, J. Metamorph. Geol. 24 (2006) 655–668.
[27] P. Lanari, A. Vho, T. Bovay, L. Airaghi, S. Centrella, Quantitative compositional mapping of mineral phases by electron probe micro-analyser, Geol. Soc. Lond. Spec. Publ. 478 (2019) 39–63.
[28] P. Lanari, O. Vidal, V. De Andrade, B. Dubacq, E. Lewin, E.G. Grosch, S. Schwartz, XMapTools: A MATLAB©-based program for electron microprobe X-ray image processing and geothermobarometry, Comput. Geosci. 62 (2014) 227–240.
[29] P. Lanari, An introduction to XMapTools. User-guide, version 2020-06-10, (2020). https://www.xmaptools.com/XMapTools.3.4_UserGuide.pdf.
[30] P. Lanari, F. Piccoli, New horizons in quantitative compositional mapping–Analytical conditions and data reduction using XMapTools, in: IOP Conf. Ser. Mater. Sci. Eng., IOP Publishing, 2020: p. 012016.
[31] G. Wellenreuther, U.E.A. Fittschen, M.E.S. Achard, A. Faust, X. Kreplin, W. Meyer-Klaucke, Optimizing total reflection X-ray fluorescence for direct trace element quantification in proteins I: Influence of sample homogeneity and reflector type, Spectrochim. Acta Part B At. Spectrosc. 63 (2008) 1461–1468.
[32] L. Sancey, V. Motto-Ros, B. Busser, S. Kotb, J.M. Benoit, A. Piednoir, F. Lux, O. Tillement, G. Panczer, J. Yu, Laser spectrometry for multi-elemental imaging of biological tissues, Sci. Rep. 4 (2014) 6065.
[33] P. Kump, K. Vogel-Mikuš, Quantification of 2D elemental distribution maps of intermediate-thick biological sections by low energy synchrotron μ-X-ray fluorescence spectrometry, J. Instrum. 13 (2018) C05014.
[34] F. Trichard, L. Sorbier, S. Moncayo, Y. Blouët, C.-P. Lienemann, V. Motto-Ros, Quantitative elemental imaging of heterogeneous catalysts using laser-induced breakdown spectroscopy, Spectrochim. Acta Part B At. Spectrosc. 133 (2017) 45–51.

667 [35] L. Jolivet, V. Motto-Ros, L. Sorbier, T. Sozinho, C.-P. Lienemann, Quantitative imaging of
668 carbon in heterogeneous refining catalysts, J. Anal. At. Spectrom. 35 (2020) 896–903.
669 [36] P. Veber, K. Bartosiewicz, J. Debray, G. Alombert-Goget, O. Benamara, V. Motto-Ros, M.P.
670 Thi, A. Borta-Boyon, H. Cabane, K. Lebbou, Lead-free piezoelectric crystals grown by the
671 micro-pulling down technique in the BaTiO 3–CaTiO 3–BaZrO 3 system, CrystEngComm. 21
672 (2019) 3844–3853.
673 [37] J. Cauzid, GEOCHIMIE ET IMAGERIE X DES FLUIDES INCLUS DANS LES SYSTEMES
674 HYDROTHERMAUX FOSSILES : DEVELOPPEMENTS EXPERIMENTAUX., Université
675 Paris 7, 2005.
676 [38] S. Pessanha, A. Guilherme, M.L. Carvalho, Comparison of matrix effects on portable and
677 stationary XRF spectrometers for cultural heritage samples, Appl. Phys. A. 97 (2009) 497–505.
678 https://doi.org/10.1007/s00339-009-5251-x.
679 [39] A. Tarantola, P. Voudouris, A. Eglinger, C. Scheffer, K. Trebus, M. Bitte, B. Rondeau, C.
680 Mavrogonatos, I. Graham, M. Etienne, C. Peiffert, Metamorphic and Metasomatic Kyanite-
681 Bearing Mineral Assemblages of Thassos Island (Rhodope, Greece), Minerals. 9 (2019) 252.
682 [40] K. Trebus, A. Tarantola, C. Fabre, M.-C. Caumon, P. Voudouris, A combined μLIBS, μXRF,
683 EPMA, cathodoluminescence, Raman spectroscopy study of blue-green zoned kyanite of
684 Thassos island (Rhodope, Greece), Appl. Spectrosc. (in prep).
685 [41] A.J. Wojtowicz, Luminescence of Cr3+ in kyanite, J. Lumin. 50 (1991) 221–230.
686 https://doi.org/10.1016/0022-2313(91)90046-X.
687 [42] M. Gaft, L. Nagli, G. Panczer, G.R. Rossman, R. Reisfeld, Laser-induced time-resolved
688 luminescence of orange kyanite Al2SiO5, Opt. Mater. 33 (2011) 1476–1480.
689 https://doi.org/10.1016/j.optmat.2011.03.052.
690 [43] R. Castaing, Application des sondes électroniques à une méthode d'analyse ponctuelle chimique
691 et cristallographique, These Univ. Paris 1951. (1952).
692 [44] V. Motto-Ros, D. Syvilay, L. Bassel, E. Negre, F. Trichard, F. Pelascini, J. El Haddad, A.
693 Harhira, S. Moncayo, J. Picard, D. Devismes, B. Bousquet, Critical aspects of data analysis for
694 quantification in laser-induced breakdown spectroscopy, Spectrochim. Acta Part B At.
695 Spectrosc. 140 (2018) 54–64. https://doi.org/10.1016/j.sab.2017.12.004.
696 [45] V.A. Solé, E. Papillon, M. Cotte, Ph. Walter, J. Susini, A multiplatform code for the analysis of
697 energy-dispersive X-ray fluorescence spectra, Spectrochim. Acta Part B At. Spectrosc. 62 (2007)
698 63–68. https://doi.org/10.1016/j.sab.2006.12.002.
699 [46] V. De Andrade, J. Ganne, B. Dubacq, C.G. Ryan, F. Bourdelle, A. Plunder, G. Falkenberg, J.
700 Thieme, Retrieving past geodynamic events by unlocking rock archives with μ-XRF and μ-
701 spectroscopy, in: J. Phys. Conf. Ser., Brookhaven National Laboratory (BNL), 2014.
702 [47] R. Tauler, Multivariate curve resolution applied to second order data, Chemom. Intell. Lab. Syst.
703 30 (1995) 133–146.
704 [48] A. Nardecchia, C. Fabre, J. Cauzid, F. Pelascini, V. Motto-Ros, L. Duponchel, Detection of
705 minor compounds in complex mineral samples from millions of spectra: A new data analysis
706 strategy in LIBS imaging, Anal. Chim. Acta. 1114 (2020) 66–73.
707 https://doi.org/10.1016/j.aca.2020.04.005.
708 [49] A. Nardecchia, C. Fabre, J. Cauzid, F. Pelascini, V. Motto-Ros, L. Duponchel, Detection of
709 minor compounds in complex mineral samples from millions of spectra: A new data analysis
710 strategy in LIBS imaging, Anal. Chim. Acta. (2020).
711 [50] H. Meyer, J. Cauzid, hameye/MARCIA: MARCIA v 0.1.0, Zenodo, 2020.
712 https://doi.org/10.5281/ZENODO.3929745.
713

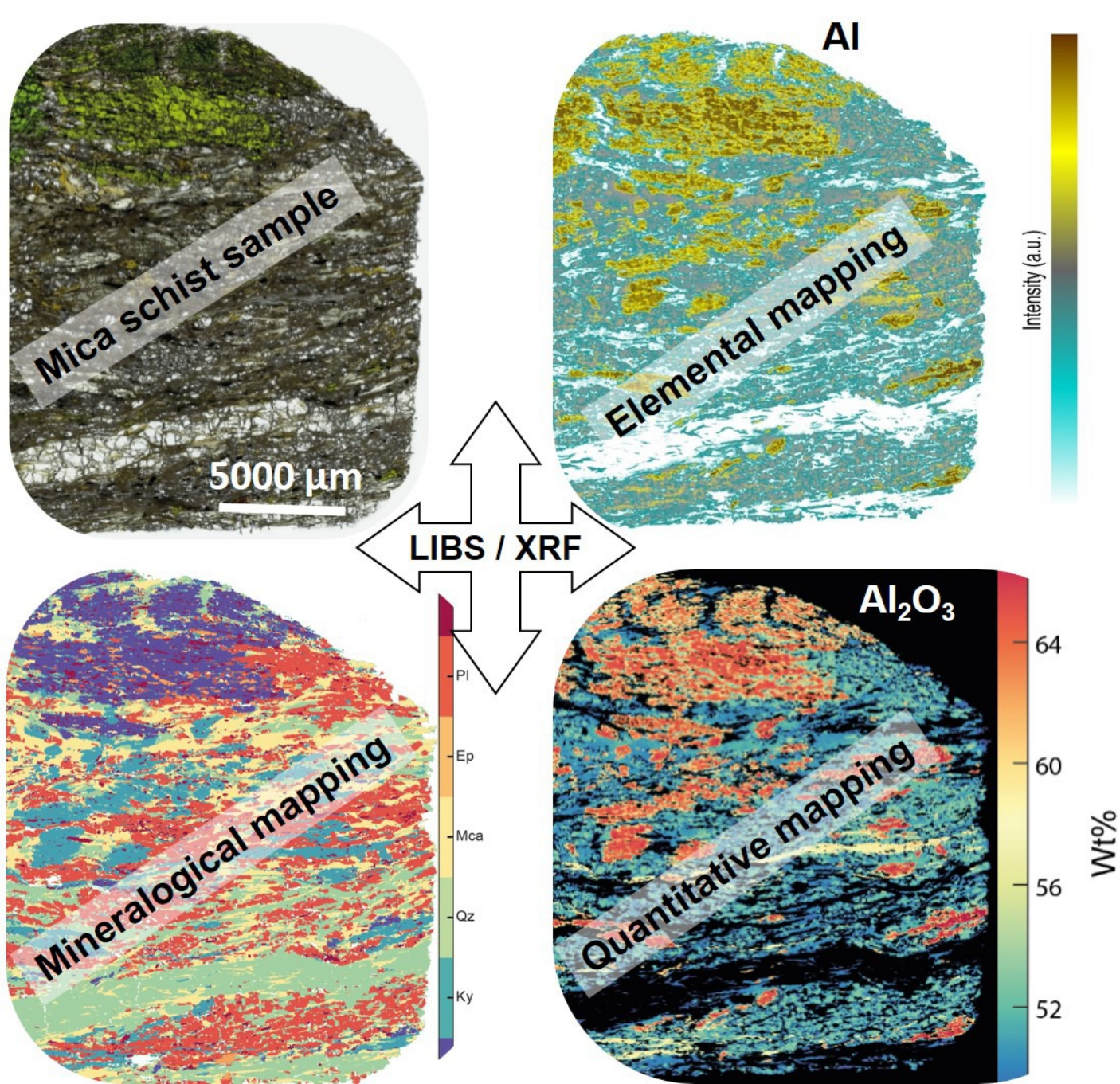
Mica schist sample
5000 µm
Al
Elemental mapping
Intensity (a.u.)
LIBS / XRF
Mineralogical mapping
Pl
Ep
Mca
Qz
Ky
Al_2O_3
Quantitative mapping
64
60
56
52
Wt%